USGS
science for a changing world

U.S. Department of the Interior
U.S. Geological Survey

Scientific Investigations Map 3446
Supersedes USGS Scientific Investigations Map 3064

Seismicity of the Earth 1900–2018

By Gavin P. Hayes,[1] Gregory M. Smoczyk,[1] Antonio H. Villaseñor,[2] Kevin P. Furlong,[3] and Harley M. Benz[1]

[1]U.S. Geological Survey
[2]ICTJA-CSIC, Institute of Earth Sciences Jaume Almera, Barcelona, Spain
[3]Department of Geosciences, Pennsylvania State University, State College, Penn.

Suggested citation: Hayes, G.P., Smoczyk, G.M., Villaseñor, A.H., Furlong, K.P., and Benz, H.M., 2020, Seismicity of the Earth 1900–2018: U.S. Geological Survey Scientific Investigations Map 3446, scale 1:22,500,000, https://doi.org/10.3133/sim3446.
[Supersedes USGS Scientific Investigations Map 3064.]

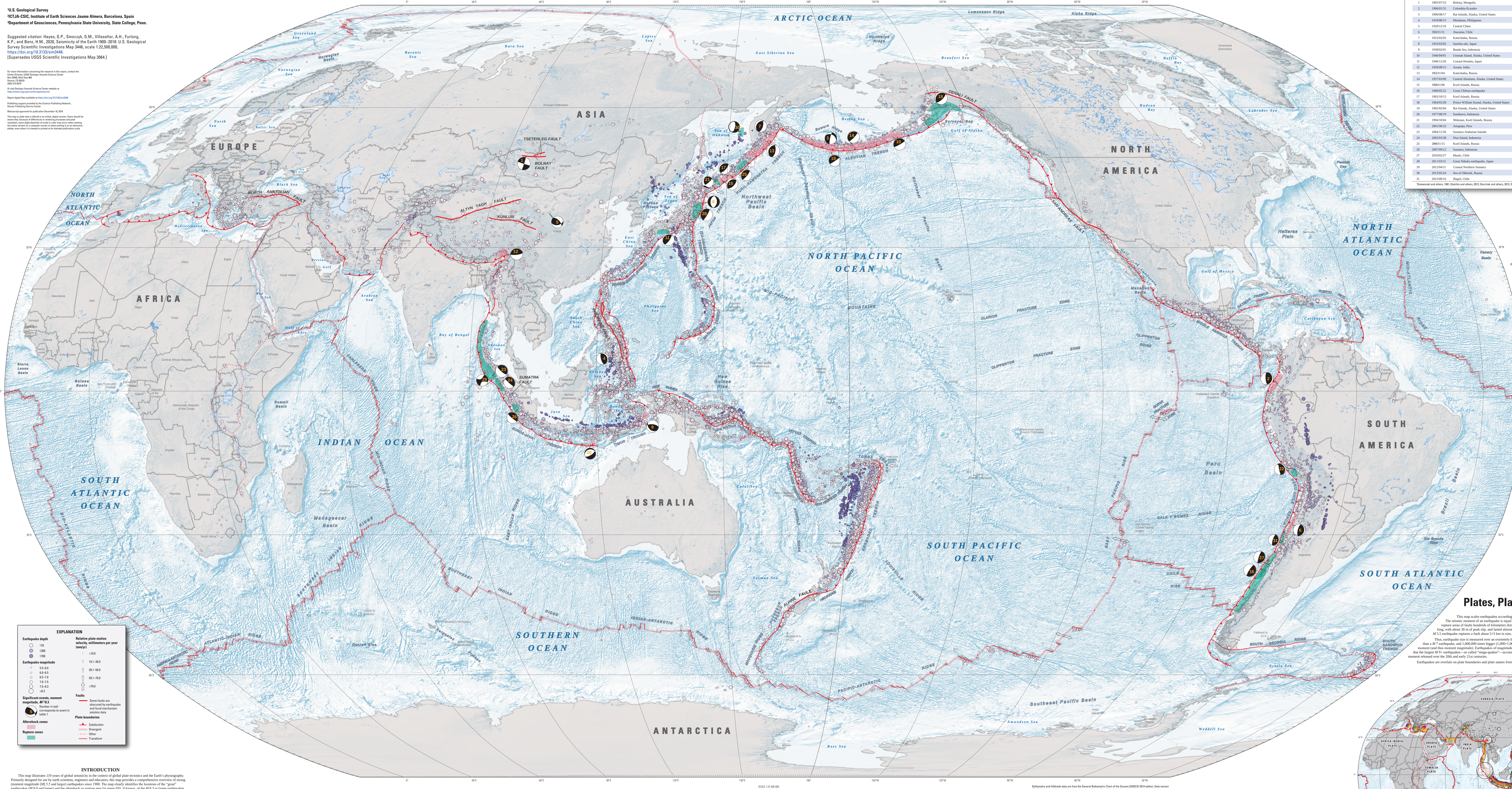

Table 1. Great Earthquakes ($M_w \geq 8.3$) 1900–2018

[Date given in year/month/day format; Moment (Newton-meters [N m]); M_w, moment magnitude; Mechanism S/D/R, strike/dip/rake of one plane of the focal mechanism solution; Global CMT, The global centroid-moment-tensor project, (https://www.globalcmt.org/); PDE, Preliminary determination of epicenters; NEIC, U.S. Geological Survey National Earthquake Information Center (https://www.usgs.gov/centers/geohazards/about/national-earthquake-information-center-neic); M_{ww}, moment W-phase magnitude]

Event	Date	Name	Moment 1×10^{21} (N m)	M_w	Moment reference	Mechanism (S/D/R)	Mechanism reference	Rupture area reference
1	1905/07/23	Bolnay, Mongolia	3.97	8.3	Schlupp and Cisternas (2007)	90/87/4	Schlupp and Cisternas (2007)	Schlupp and Cisternas (2007)
2	1906/01/31	Colombia-Ecuador	20.4	8.8	Kanamori (1977)	30/20/120	Swenson and Beck (1999), Kanamori and Given (1981)	Kanamori and McNally (1982)
3	1906/08/17	Rat Islands, Alaska, United States	3.80	8.3	Okal (2005)	196/80/-56	Okal (2005)	Area of the circle determined from moment magnitude
4	1918/08/15	Mindanao, Philippines	3.00	8.3	Okal and others (2011)	327/22/69	Okal and others (2011)	Okal and others (2011)
5	1920/12/16	Central China	3.00	8.3	Chen and Molnar (1977)	70/45/45	Chen and Molnar (1977)	Chen and Molnar (1977)
6	1922/11/11	Atacama, Chile	6.90	8.5	Kanamori (1977)	0/20/90	Beck and others (1998)	Kelleher (1972)
7	1923/02/03	Kamchatka, Russia	5.50	8.4	Okal (1992)	214/30/110	Kanamori (1976)	Johnson and Satake (1999)
8	1933/03/02	Sanriku-oki, Japan	4.30	8.4	Okal (1992)	180/45/-90	Kanamori (1971)	Kawakatsu and Seno (1983)
9	1938/02/01	Banda Sea, Indonesia	8.37	8.6	Okal and Reymond (2003)	276/63/70	Okal and Reymond (2003)	Area of the circle determined from moment magnitude
10	1946/04/01	Unimak Island, Alaska, United States	8.50	8.6	López and Okal (2006)	250/6/90	López and Okal (2006)	Area is determined from aftershock distribution
11	1946/12/20	Coastal Honshu, Japan	4.00	8.3	Kato and Ando (1997)	245/17/119	Kato and Ando (1997)	Kato and Ando (1997)
12	1950/08/15	Assam, India	10.0	8.6	Kanamori (1977)	260/12/90	Chen and Molnar (1977)	Kumar and others (2006)
13	1952/11/04	Kamchatka, Russia	35.0	9.0	Kanamori (1977)	214/30/110	Kanamori (1976)	Johnson and Satake (1999)
14	1957/03/09	Central Aleutians, Alaska, United States	8.80	8.6	Johnson and others (1994)	257/11/116	Johnson and Satake (1993)	Wyss and Wiemer (1999)
15	1958/11/06	Kuril Islands, Russia	4.00	8.3	Kanamori (1977)	225/30/90	Fukao and Furumoto (1979)	Area is determined from aftershock distribution
16	1960/05/22	Great Chilean earthquake	200.0	9.5	Kanamori (1977)	10/10/80	Kanamori and Cipar (1974)	Moreno and others (2009)
17	1963/10/13	Kuril Islands, Russia	6.70	8.5	Kanamori (1977)	223/22/90	Kanamori (1970a)	Beck and Ruff (1987)
18	1964/03/28	Prince William Sound, Alaska, United States	82.0	9.2	Kanamori (1977)	246/20/90	Kanamori (1970b)	Suito and Freymueller (2009)
19	1965/02/04	Rat Islands, Alaska, United States	12.5	8.7	Kanamori (1977)	290/10/139	Wu and Kanamori (1973)	Beck and Christensen (1991)
20	1977/08/19	Sumbawa, Indonesia	3.59	8.3	Global CMT[1]	260/24/-73	Global CMT[1]	Spence (1986)
21	1994/10/04	Shikotan, Kuril Islands, Russia	3.43	8.3	PDE, Duputel and others (2012)	158/34/21	PDE, Duputel and others (2012)	Hayes (2017)
22	2001/06/23	Arequipa, Peru	4.95	8.4	PDE, Duputel and others (2012)	315/16/70	PDE, Duputel and others (2012)	Hayes (2017)
23	2004/12/26	Sumatra-Andaman Islands	66.8	9.2	Park and others (2005)	329/8/110	PDE, Duputel and others (2012)	Ammon and others (2005)
24	2005/03/28	Nias Island, Indonesia	8.88	8.6	PDE/NEIC M_{ww}	329/11/107	PDE/NEIC M_{ww}	Hayes (2017)
25	2006/11/15	Kuril Islands, Russia	3.37	8.3	PDE, Duputel and others (2012)	208/16/83	PDE, Duputel and others (2012)	Hayes (2017)
26	2007/09/12	Sumatra, Indonesia	5.30	8.4	PDE, Duputel and others (2012)	323/11/103	PDE, Duputel and others (2012)	Hayes (2017)
27	2010/02/27	Maule, Chile	22.6	8.8	PDE, Duputel and others (2012)	17/14/108	PDE, Duputel and others (2012)	Hayes (2017)
28	2011/03/11	Great Tohoku earthquake, Japan	55.9	9.1	PDE, Duputel and others (2012)	193/9/78	PDE, Duputel and others (2012)	Hayes (2017)
29	2012/04/11	Coastal Northern Sumatra	8.92	8.6	PDE/NEIC M_{ww}	199/80/5	PDE/NEIC M_{ww}	Meng and others (2012)
30	2013/05/24	Sea of Okhotsk, Russia	3.84	8.3	PDE/NEIC M_{ww}	184/10/-98	PDE/NEIC M_{ww}	Ye and others (2013)
31	2015/09/16	Illapel, Chile	3.19	8.3	PDE/NEIC M_{ww}	353/19/83	PDE/NEIC M_{ww}	Hayes (2017)

[1]Dziewonski and others, 1981; Ekström and others, 2012; Storchak and others, 2013, Storchak and others, 2015; and Di Giacomo and others, 2018.

Seismic Hazard Near Populated Areas

Many areas of the planet with high seismic hazard are also heavily populated. The map to the right illustrates the relationship between population and earthquake hazard in Asia and the western Pacific by extruding exaggerated population density (grayscale three-dimensional tetrahedra) and overlaying the Global Earthquake Model (GEM) Global Mosaic of Hazard Models (Pagani and others, 2018). The view point is from elevation above the central Pacific Ocean, looking west. The higher the three-dimensional (3D) extrusion, the larger the local population density. Hazard is depicted as the level of peak ground acceleration (PGA) with a 10 percent probability of being exceeded in 50 years, equivalent to a return period of 475 years. Warm colors represent high seismic hazard, shades of green represent moderate hazard, while blue-to-transparent colors represent low hazard. In the background where no color is visible, there is a very low level of hazard. Here, black and white represents population only; white for less dense, and black for greater density.

For example, in the foreground along coastal Japan, the large orange spike represents densely populated Tokyo, where earthquake shaking also occurs regularly and seismic hazard is high. West of Japan, the high population density of China is visible as a spikey landscape. Much of central and eastern China has low-to-moderate levels of seismic hazard (blue colors), while some densely populated cities in northern and western China are located in regions of moderate-to-high hazard (green-to-yellow colors). The large yellow spike in the center-left of the figure represents Manila, where seismic hazard is also moderate-to- high. In the background, the high hazard Himalaya region can be seen (orange-to-red swath), as can the moderate-to-high hazards in the Mediterranean region of Europe and Africa.

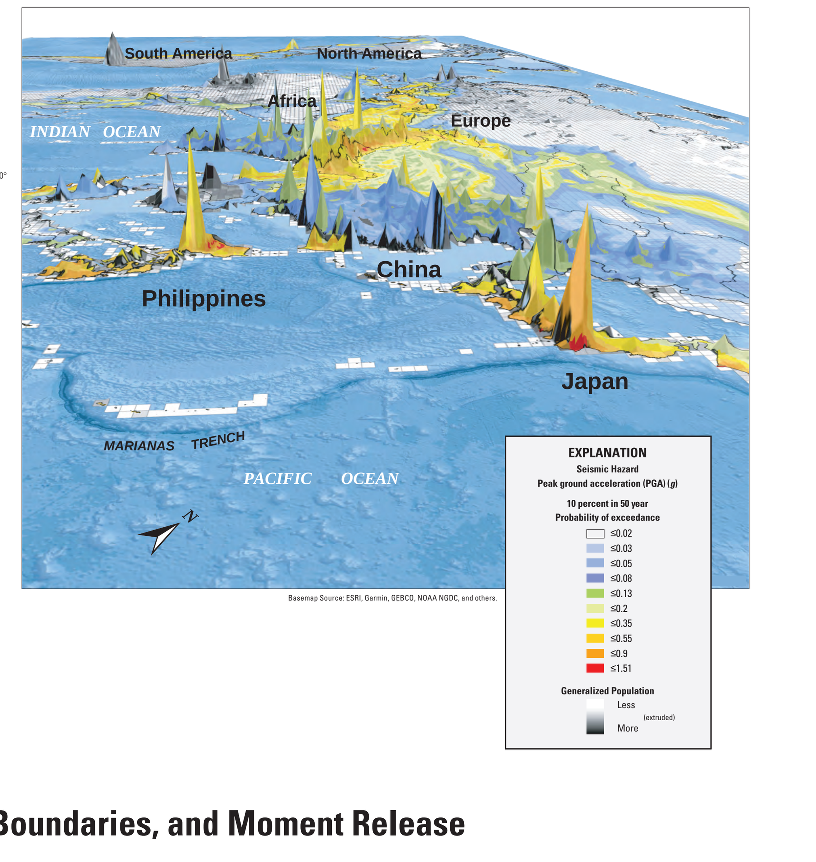

Plates, Plate Boundaries, and Moment Release

This map scales earthquakes according to their seismic moment (M_w), the basis for the moment magnitude scale used in modern seismology. The larger the circle, the greater the moment magnitude. The seismic moment of an earthquake is equal to the product of the area of a fault that ruptured during the earthquake, the amount the fault slipped, and the rigidity of the rock. The largest earthquakes (M 9+) rupture areas of faults hundreds of kilometers (km) long, more than 100 km wide, and slip for tens of meters (m) over a period of minutes. The 2004 M 9.1 Sumatra earthquake ruptured a fault about 1,300 km long, with about 30 m of peak slip, and lasted almost 10 minutes. The 2011 M 9.1 Japan earthquake ruptured a fault about 400 km long, with upwards of 75 m of slip, over 2–3 minutes. On the other hand, a typical M 5.5 earthquake ruptures a fault about 5×5 km in size, with an average slip of tens of centimeters (cm), lasting only a second or two.

Thus, earthquake size is measured over an extremely broad range of scales that can be difficult to articulate, and equally difficult to envision. Measured by its seismic moment, an M 9 earthquake is 1,000 times bigger than a M 7 earthquake, and 1,000,000 times bigger (1,000×1,000) than an M 5 event. We attempt to illustrate these differences here by sizing the earthquake symbols of the largest earthquakes according to their seismic moment (and thus moment magnitude). Earthquakes of magnitudes less than or equal to (less than or equal to [≤]) 8.1 appear as points; only the largest events have resolvable size in this display. This is consistent with the fact that the largest M 9+ earthquakes—so called "mega-quakes"—account for the vast majority of seismic moment released on the planet. The 1960 M 9.5 Great Chilean earthquake accounts for close to 25 percent of all earthquake moment released over the 20th and early 21st centuries.

Earthquakes are overlain on plate boundaries and plate names from the MORVEL plate motion model (DeMets and others, 2010), and subduction zone depth contours from the Slab2 database (Hayes and others, 2018).

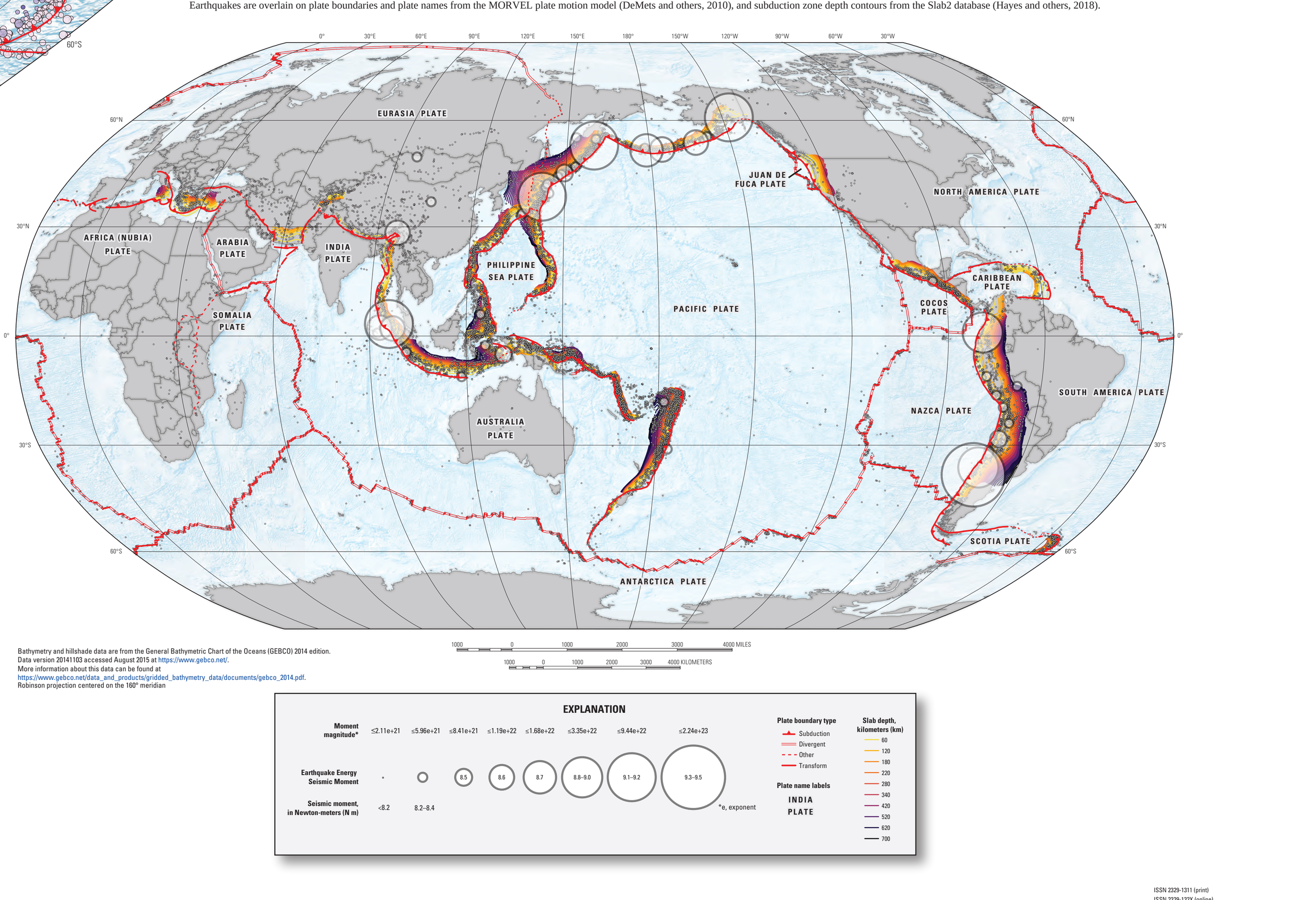

INTRODUCTION

This map illustrates 119 years of global seismicity in the context of global plate tectonics and the Earth's physiography. Primarily designed for use by earth scientists, engineers and educators, this map provides a comprehensive overview of strong (moment magnitude [M] 5.5 and larger) earthquakes since 1900. The map clearly identifies the locations of the "great" earthquakes (M 8.0 and larger) and the aftershock or rupture area (in green fill), if known, of the M 8.3 or larger earthquakes. The circular earthquake symbols are scaled to be proportional to the moment magnitude and therefore to the area of faulting, thus providing a better understanding of the relative sizes and distribution of earthquakes in the magnitude range 5.5 to 9.5. Plotting the known rupture or aftershock areas (which are closely related) of the largest earthquakes also provides a better appreciation of the faulting extent of some of the most famous and damaging instrumentally recorded earthquakes in modern history.

GLOBAL SEISMICITY AND EARTHQUAKE LOCATION PROCEDURES

The seismicity shown in this map comes from the U.S. Geological Survey's (USGS) Advanced National Seismic System (ANSS) Combined Catalog (ComCat), which in turn is derived from numerous sources that contain information on earthquake locations, magnitudes, felt areas, and damage reports. These reports and investigations span the development of modern seismological practices and the advent of plate tectonics; as a result, there was no uniform standard for the reporting of magnitudes, locations, and other seismological observations. The primary data source for pre-1973 earthquake locations and magnitudes is the ISC-GEM Global Instrumental Earthquake Catalogue (Dziewonski and others, 1981; Ekström and others, 2012; Storchak and others, 2013, Storchak and others, 2015; and Di Giacomo and others, 2018), which predominantly covers seismicity from 1904 to 2015, and also contains large (M 7.0 or greater) earthquakes from 1900 to 1904. The ISC-GEM catalog represents a specialized effort to create a uniform, standardized catalog of earthquakes that substantially improves upon other existing bulletins, specifically for the purposes of hazard modeling and seismotectonic mapping and analyses such as that presented here. Earthquake locations and seismic phase data from 1973 to present are derived from the bulletin of the USGS National Earthquake Information Center (NEIC). Here, we have combined the seismic observations from these sources to produce a global seismicity map that is complete for M ~6.5 or larger for much of the period from 1900 to 1963 and M ~5.5 or larger from 1964 to the present. Search mechanisms for seismological data contained in ComCAT can be found at https://earthquake.usgs.gov/earthquakes/search/.

RUPTURE/AFTERSHOCK ZONES

Rupture or aftershock zones and focal mechanisms are shown for 31 earthquakes with moments of 3.0×1,028 dyne-cm or larger (M 8.3 or larger). Table 1 identifies these earthquakes by the location, magnitude, and reference for each of the rupture/aftershock zones shown on the map. Rupture zones are specifically derived from finite fault modeling approaches (for example, Hayes, 2017). In the cases of earthquakes for which we do not have models of the rupture zones derived from finite-fault modeling of seismographic data, we plot the geographic regions spanned by dense distributions of earthquake aftershocks, since aftershocks tend to occur within or on the margins of rupture zones. Most of the tabulated pre-1964 earthquakes are associated with aftershock zones rather than rupture zones. These aftershock zones provide a less precise representation of fault rupture than is typical for the rupture zones inferred from finite-fault modeling of later earthquakes, both because there may not be a one-to-one correlation between aftershock locations and the interiors or margins of the main-shock fault ruptures and because of the poorer quality and sparser distribution of instrumentation over the pre-1964 time period. Rupture zones for all earthquakes after 1990 are determined from modeling the slip distribution of each earthquake following the approach of Ji and others (2002), and as described in Hayes (2017). Between 1964 and 1990, most M8.3 or greater events have rupture zones derived from finite fault modeling in independent studies (see table 1).

NEOTECTONIC PLATES, INTRAPLATE FAULTS, AND VOLCANOES

The plate boundaries shown on the map were modified from the plate boundary model (PB2002) developed by Bird (2003). We excluded a number of boundaries that Bird (2003) identified as diffuse or poorly defined. We also do not show boundaries of many small "microplates." Finally, we used different geometries for a few boundaries when revisions to Bird's (2003) model seemed justified by more recent studies. There are several examples on the map where "great" earthquakes (M 8.0 or larger) do not occur near or at the plotted plate boundary. For these cases, we also show the fault along which the earthquake occurred; examples of these are the Bolnay and Tseterleg faults in central Mongolia. Some other major continental faults that have produced large earthquakes are also labeled, such as the Anatolian fault in Turkey and the Denali fault in Alaska.

REFERENCES CITED

Ammon, C.J., Ji, C., Thio, H.-K., Robinson, D., Ni, S., Hjorleifsdottir, V., Kanamori, H., Lay, T., Das, S., Helmberger, D., Ichinose, G., Polet, J., and Wald, D., 2005, Rupture process of the 2004 Sumatra-Andaman earthquake: Science, v. 308, no. 5725, p. 1133–1139. [Also available at https://doi.org/10.1126/science.1112260.]

Beck, S.L., Barrientos, S., Kausel, E., and Reyes, M., 1998, Source characteristics of historic earthquakes along the central Chile subduction zone: Journal of South American Earth Sciences, v. 11, no. 2, p. 115–129. [Also available at https://doi.org/10.1016/S0895-9811(98)00005-4.]

Beck, S.L., and Christensen, D.H., 1991, Rupture process of the February 4, 1965, Rat Islands earthquake: Journal of Geophysical Research, v. 96, no. B2, p. 2205–2221. [Also available https://doi.org/10.1029/90JB02092.]

Beck, S.L., and Ruff, L.J., 1987, Rupture process of the great 1963 Kurile Islands earthquake sequence—Asperity interaction and multiple event rupture: Journal of Geophysical Research, v. 92, no. B13, p. 14123–14138. [Also available at https://doi.org/10.1029/JB092iB13p14123.]

Bird, P., 2003, An updated digital model of plate boundaries: Geochemistry, Geophysics, Geosystems, v. 4, no. 3, 52 p. [Also available at https://doi.org/10.1029/2001GC000252.]

Chen, W-P., and Molnar, P., 1977, Seismic moments of major earthquakes and average rate of slip in central Asia: Journal of Geophysical Research, v. 82, no. 20, p. 2945–2969. [Also available at https://doi.org/10.1029/JB082i020p02945.]

DeMets, C., Gordon, R.G., and Argus, D.F., 2010, Geologically current plate motions: Geophysical Journal International, v. 181, no. 1, p. 1–80. [Also available at https://doi.org/10.1111/j.1365-246X.2009.04491.x.]

Di Giacomo, D., Engdahl, E.R., and Storchak, D.A., 2018, The ISC-GEM earthquake catalogue (1904–2014)—Status after the extension project: Earth System Science Data, v. 10, no. 4, p. 1877–1899, accessed Sept. 1, 2019, at https://doi.org/10.31905/D808B825.

Duputel, Z., Rivera, L., Kanamori, H., and Hayes, G., 2012, W phase source inversion for moderate to large earthquakes (1990–2010): Geophysical Journal International, v. 189, no. 2, p. 1125–1147. [Also available at https://doi.org/10.1111/j.1365-246X.2012.05419.x.]

Wu, F.T., and Kanamori, H., 1973, Source mechanism of February 4, 1965, Rat Island earthquake: Journal of Geophysical Research, v. 78, no. 26, p. 6082–6092. [Also available at https://doi.org/10.1029/JB078i026p06082.]

Wyss, M., and Wiemer, S., 1999, How can one test the seismic gap hypothesis? The case of repeated ruptures in the Aleutians, in Wyss, M., Shimazaki, K., and Ito, A, eds., Seismicity patterns, their statistical significance and physical meaning: Basel, Switzerland, Pure and Applied Geophysics, Pageoph Topical Volumes, v. 155, p. 259–278, Birkhäuser. [Also available at https://doi.org/10.1007/978-3-0348-8677-2_4.]

Ye, L., Lay, T., Kanamori, H., and Koper, K., 2013, Energy release of the 2013 M_w 8.3 Sea of Okhotsk earthquake and deep slab stress heterogeneity: Science, v. 341, no. 6152, p. 1380–1384, accessed Sept. 1, 2019, at https://doi.org/10.1126/science.1242032.

Schematic Diagram of a Focal Mechanism

Seismologists refer to the direction of slip in an earthquake and the orientation of the fault on which it occurs as the *focal mechanism*. They use information from seismograms to calculate the focal mechanism and typically display it on maps as a "beach ball" symbol, as shown in part *A*. This symbol is the projection on a horizontal plane of the lower half of an imaginary, spherical shell (*focal sphere*) surrounding the earthquake source. A line is scribed where the fault plane intersects the shell. The stress field orientation at the time of rupture governs the direction of slip on the fault plane; the beach ball depicts this stress orientation through shading. The black quadrants contain the tension axis (*T*), which reflects the minimum stress direction, and the white quadrants contain the pressure axis (*P*), which reflects the maximum stress direction.
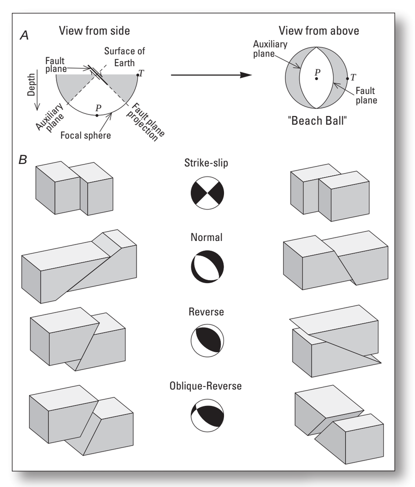
For mechanisms calculated from the first-motion direction of seismograms, there is an ambiguity in identifying the fault plane on which slip occurred from the orthogonal, mathematically equivalent, *auxiliary* plane. In part *B*, we illustrate this ambiguity with four examples. The block diagrams adjacent to each focal mechanism illustrate the two possible types of fault motion that the focal mechanism could represent. Note that the view angle is 30° to the left of and above each diagram. The ambiguity may be resolved by comparing the two fault plane orientations to the alignment of small earthquakes and aftershocks shown in map and cross-section views. The first three examples describe fault motion that is purely horizontal (*strike-slip*) or vertical (*normal or reverse*). The *oblique- reverse* mechanism illustrates that slip may also have components of horizontal and vertical motion.